PAPER • OPEN ACCESS

Light-induced charge transfer at the CH$_3$NH$_3$PbI$_3$/TiO$_2$ interface—a low-temperature photo-electron paramagnetic resonance assay

To cite this article: Konstantins Mantulnikovs *et al* 2020 *J. Phys. Photonics* **2** 014007

View the article online for updates and enhancements.

JPhys Photonics

PAPER

Light-induced charge transfer at the CH$_3$NH$_3$PbI$_3$/TiO$_2$ interface—a low-temperature photo-electron paramagnetic resonance assay

Konstantins Mantulnikovs[1] , Péter Szirmai[1] , Márton Kollár[1] , Jeremy Stevens[1,4], Pavao Andričević[1], Anastasiia Glushkova[1], Lidia Rossi[1], Philippe Bugnon[2], Endre Horváth[1], Andrzej Sienkiewicz[1,3] , László Forró[1] and Bálint Náfrádi[1]

1   Laboratory of Physics of Complex Matter, École Polytechnique Fédérale de Lausanne, CH-1015 Lausanne, Switzerland
2   Institute of Physics, École Polytechnique Fédérale de Lausanne, CH-1015 Lausanne, Switzerland
3   ADSresonances Sàrl, Route de Genève 60B, CH-1028 Préverenges, Switzerland
4   Present address: Université Lyon, ENS de Lyon, Université Claude Bernard Lyon 1, CNRS, Laboratoire de Physique, F-69342 Lyon, France.

E-mail: peter.szirmai@epfl.ch and andrzej.sienkiewicz@epfl.ch

Abstract

The performance of organic–inorganic metal halide perovskites-based (MHPs) photovoltaic devices critically depends on the design and material properties of the interface between the light-harvesting MHP layer and the electron transport layer (ETL). Therefore, the detailed insight into the transfer mechanisms of photogenerated carriers at the ETL/MHP interface is of utmost importance. Owing to its high charge mobilities and well-matched band structure with MHPs, titanium dioxide (TiO$_2$) has emerged as the most widely used ETL material in MHPs-based photovoltaic devices. Here, we report a contactless method to directly track the photo-carriers at the ETL/MHP interface using the technique of low-temperature electron paramagnetic resonance (EPR) in combination with *in situ* illuminations (Photo-EPR). Specifically, we focus on a model nanohybrid material consisting of TiO$_2$-based nanowires (TiO$_2$NWs) dispersed in the polycrystalline methylammonium lead triiodide (MAPbI$_3$) matrix. Our approach is based on observation of the light-induced decrease in intensity of the EPR signal of paramagnetic Ti^{3+} ($S = 1/2$) in non-stoichiometric TiO$_2$NWs. We associate the diminishment of the EPR signal with the photo-excited electrons that cross the ETL/MHP interface and contribute to the conversion of Ti^{3+} states to EPR-silent Ti^{2+} states. Overall, we infer that the technique of low-temperature Photo-EPR is an effective strategy to study the transfer mechanisms of photogenerated carriers at the ETL/MHP interface in MAPbI$_3$-based photovoltaic and photoelectronic systems.

1. Introduction

Recently, organic–inorganic metal halide perovskites (MHPs) have attracted considerable attention in various domains of optoelectronics, including light emission, sensing and photovoltaics (see [1] and references therein), due to their excellent photophysical properties, such as high light absorption coefficient, technologically-tunable bandgap, absence of deep trap states within the bandgap, high charge mobility and long diffusion lengths as well as excellent photoluminescence quantum yield.

Such a variety of attractive properties of MHPs accompanied also by their low-cost solution processability, sparked the interest to use these materials in a large number of optoelectronic systems [2, 3]. Currently, the most prominent implementations are solar cells [4], lasers [5] and light-emitting diodes [6].

Recent advances in technologies of preparation and processing of MHPs largely enhanced the conversion of solar energy into an electrical current. Consequently, over a period of only a few years, MHPs-based solar cells have seen a remarkable rise in power conversion efficiencies (PCEs) from the initial 3.8% [7] and 9.7% [8] to the

currently certified record of 25.2% [9]. Specifically, due to better engineering of the electron and hole transport layers (hereinafter ETLs and HTLs), the charge extraction from MHPs has been significantly improved.

In parallel to applications in photovoltaics, a number of studies have also investigated a variety of MHPs-based detectors and sensors, including x-ray detecting devices [10], near-ultraviolet to near-infrared (330–800 nm) light detectors [5, 11–13], tactile sensors [14], as well as gas [15] and even high-energy particle detectors [16].

In general, the above-mentioned devices were designed as planar structures. Therefore, for serving specific purposes, their architectures required a stack of various kinds of functional thin layers. In consequence, besides MHP-based light-harvesting layers, the other most investigated elements of the stacked planar architectures were the ETLs and HTLs, as well as the device terminal electrodes [11, 17–21].

Despite recent progress in the technology of functional layers and device configurations, TiO_2 is still most commonly used for designing ETLs in MHP-based devices. TiO_2 offers a number of important advantages, including chemical stability, nontoxicity, high charge mobilities, well-matched band structure with MHPs, low-cost and simple fabrication procedures [22]. It has been shown that the performance of TiO_2-based ETLs could be largely improved through bandgap-engineering by doping with transition metal [23] or nonmetal elements [24, 25], surface functionalization [26], photosensitization [27] and heterojunction preparation [28]. In fact, the recent surge of interest in perovskite-based devices opened a new research area oriented towards optimization of both the physicochemical properties of TiO_2 itself and the morphology of its interface with MHPs.

The archetypal halide perovskite and also the first successfully employed MHP in solar cells, methylammonium lead triiodide, $CH_3NH_3PbI_3$ (hereinafter $MAPbI_3$), is continuing to be used as a model material to study the transfer mechanisms of light-generated carriers in various types of bilayer MHP/ETL or MHP/ HTL systems [29–31].

There have been several reports on the transfer mechanisms of photogenerated carriers at the interfaces between MHPs and the electron-transporting materials, such as TiO_2, or hole-transporting materials, such as Spiro-OMeTAD or PCBM [32–34]. Time-resolved techniques, such as transient absorption (TA), photoluminescence (TRPL), and terahertz absorption (TRTS) spectroscopies, or time-resolved microwave photoconductivity (TRMC) were the most popular approaches used in these investigations [35].

Despite intensive research, the direct observation of the transfer of photogenerated carriers at the MHP/ETL interface still remains a challenge. This complicates gaining insight into the role of surface and bulk defects at the MHP/ETL interface and to better understand their influence on the device performance.

Therefore, in this work, we aim to advance the understanding of the charge transfer mechanisms of light-generated carriers in bilayer MHP/ETL systems. In particular, we show that the technique of electron paramagnetic resonance (EPR) in combination with *in situ* illuminations (Photo-EPR) can be used to directly monitor the charge transfer from $MAPbI_3$ to TiO_2, as well as to determine the exact number of trapped electrons by the TiO_2 surface defects.

Specifically, we report a low-temperature Photo-EPR study performed on a model nanohybrid system consisting of TiO_2 nanowires (TiO_2NWs) dispersed in a polycrystalline $MAPbI_3$ matrix. Our approach is based on observation of the light-induced decrease in intensity of the EPR signal of paramagnetic species of trivalent titanium (Ti^{3+}, $S = 1/2$) in TiO_2NWs. Prior to low-temperature EPR measurements, in order to enhance the concentration of Ti^{3+} species, TiO_2NWs were thermally-reduced in hydrogen (H_2) atmosphere. The thermal reduction process resulted not only in the formation of a large concentration of Ti^{3+} centers but was also accompanied by a marked colour change of the TiO_2NWs: from white to blue. Therefore, hereinafter, non-reduced (oxidized) TiO_2NWs and thermally-reduced TiO_2NWs, are referred to as white-TiO_2NWs and blue-TiO_2NWs, respectively.

The observed diminishment of the EPR signal upon illumination with the green laser light ($\lambda_{exc} = 532$ nm) is associated with the photo-excited electrons that cross the MHP/ETL interface between the grains of polycrystalline $MAPbI_3$ and dispersed blue-TiO_2NWs, thus leading to the conversion of paramagnetic states of Ti^{3+} to the EPR-silent Ti^{2+} states. We also demonstrate that a combination of the low-temperature Photo-EPR with light modulation and lock-in detection allows one to gain additional insight into the temporal evolution of the photo-excited carriers at the MHP/ETL interface. With using both techniques we successfully identified that ~20% of the surface species in blue-TiO_2NWs trapped photogenerated electrons.

Furthermore, to prove the validity of our Photo-EPR-based approach, we also set up a complementary proof-of-principle study centered on a visible light photodetector, which was designed around a junction formed between a single crystal of $MAPbI_3$ and compacted TiO_2 powder. Specifically, to make it function as a light detector, a single $MAPbI_3$ crystal was brought into electrical contact with a pellet made from TiO_2NWs. We found that the diode-like performance of this simple photodetector was markedly dependent on the type of TiO_2NWs used to form the pellet. In particular, both the forward photo-current and the rectification ratio were largely improved while employing the pellet made of blue-TiO_2NWs as compared to the pellet formed from white-TiO_2NWs. These two factors, resulting from an improved electrical conductivity and concomitant

enhanced charge extraction from MAPbI$_3$, contributed to a higher light-sensitivity of the photodetector consisting of a single crystal of MAPbI$_3$ and the pellet made of blue-TiO$_2$NWs.

2. Experimental methods

2.1. Preparation of a stoichiometric solution of MAPbI$_3$

Firstly, prior to preparing the saturated DMF solutions of MAPbI$_3$ it was necessary to prepare stoichiometric single crystals. Accordingly, MAPbI$_3$ single crystals were made by precipitation from an aqueous solution of concentrated hydroiodic acid (57 wt% in H$_2$O), containing stoichiometric amounts of lead(II) acetate trihydrate (Pb(ac)$_2$ · 3H$_2$O) and methylamine (CH$_3$NH$_2$, 40 wt% in H$_2$O). MAPbI$_3$ crystals were grown and recrystallized in the saturated hydroiodic acid solution applying temperature gradient in the vessel. The crystals were dissolved at the higher temperature side of the vessel and recrystallized at the lower temperature side of the vessel [10]. Subsequently, the obtained MAPbI$_3$ single crystals were harvested, dried at 120 °C and dissolved in DMF, leading to a 30 wt% DMF stock solution.

2.2. Opto-electronic characterization of the interface of MAPbI$_3$ and TiO$_2$NWs

The junctions in between MAPbI$_3$ and different versions of TiO$_2$NWs have been characterized by means of two-point resistance measurements at ambient conditions. One of the tungsten probe electrode needles has been placed on top of the MAPbI$_3$ crystal, pressing it against a white or blue TiO$_2$ pellet, while the second needle has been placed on the TiO$_2$ pellet, close to the crystal. A Keithley 2400 source meter allows for measurements of the current with <0.1 nA resolution while tuning the applied bias voltage. All measurements were made under white light illumination using a light intensity of 1.02 mW cm^2.

For all opto-electronic characterization experiments, we used the same MAPbI$_3$ crystal and identical electrode configurations.

2.3. Preparation of blue-TiO$_2$NWs samples

Protonated titanate (H$_2$Ti$_3$O$_7$) nanowires were prepared by a two-step hydrothermal process. The details about the typical synthesis procedure are given elsewhere [36]. As described in [37], the white powder of layered protonated titanate nanowires (TiO$_2$NWs) is heat-treated in H$_2$ flow at 600 °C for 1h. The cyan coloured hydrogenated titanium oxide nanowires (blue-TiO$_2$NWs) product was cooled fast to room temperature. Heat treatment of blue-TiO$_2$NWs in the air at 450 °C or 550 °C for 30 min resulted in white TiO$_2$NWs. The colour change from cyan to white is instantaneous upon heat treatment.

2.4. Synthesis of reduced TiO$_2$ single crystals

High-quality single crystals of blue TiO$_2$ anatase were produced by a chemical transport method from anatase powder using ammonium chloride (NH$_4$Cl) as a transport agent, following a modified procedure based on the one described in [38]. In brief, ~3.0 g of high-purity sintered powder of anatase (99.6% pure, 3–6 mm sized grains, from Merck) were sealed together with ~0.4 g of NH$_4$Cl (Merck) in a ~20 cm long, 2.0 cm in diameter, quartz ampule. Before sealing, the reagents were thoroughly dried out and evacuated at pressure <4 × 10^{-6} mbar during one night.

Subsequently, the sealed ampule was placed in a horizontal tubular two-zone furnace and heated slowly to 750 °C and 600 °C, at the source and the deposition zones, respectively. After 5–8 weeks, millimeter-sized crystals (~1.5 × 1.5 × 1.5 mm^3) with a bi-pyramidal shape were collected.

The microcrystalline powder (0.01–0.5 mm average grain sizes) of blue TiO$_2$ anatase was obtained by careful grinding of two-three small (ca. 2–3 mm^3) single crystals of blue TiO$_2$ anatase in an agate mortar. The ground material conserved the same deep-blue colour as the starting monocrystalline blue TiO$_2$ anatase.

2.5. Preparation of MAPbI$_3$/TiO$_2$ nanohybrid material

To prepare the nanohybrid structures, we mixed 20 mg of the TiO$_2$ samples (ground TiO$_2$ crystallites, white- and blue-TiO$_2$NWs powder, or Tayca Corp. AMT-600 anatase powder) with 100 μl of MAPbI$_3$ precursor solution. The nanohybrid of MAPbI$_3$ and TiO$_2$ samples were coated on the surface of $d = 2$ mm diameter quartz rods serving as light guides.

Due to a substantial difference in refractive indices between MAPbI$_3$ ($n \approx 2.8$) [39], TiO$_2$ ($n \approx 2.6$) [40] and quartz ($n \approx 1.46$) [41] our approach made it possible to efficiently extract light from the quartz light guide to the whole surface of the deposited material. Figure 3(b) provides exemplary proof of very efficient extraction of the green laser light ($\lambda_{exc} = 532$ nm) from the quartz-made sample holder to a thin deposit of white-TiO$_2$NWs.

For reference measurements, TiO$_2$ samples (ground TiO$_2$ crystallites, white- and blue-TiO$_2$NWs powder, or Tayca Corp. AMT-600 anatase powder) were mixed with 1 mg of polyethylene oxide (PEO, 100 000 MW) and

supplemented with 90% of ethanol and 10% distilled water to make a suspension. The mixture was then used to coat the $d = 2$ mm quartz rods implemented as light guides for illumination experiments.

Here, we do not implement MAPbI$_3$ as a reference sample, as our previous investigations showed that MAPbI$_3$ remained EPR-silent both in the dark and under illumination [42].

2.6. EPR experiments

Low-temperature continuous-wave ESR measurements were carried out with a Bruker ESR spectrometer E500 EleXsys Series (Bruker Biospin GmbH) equipped with a Gunn diode-based microwave bridge (model SuperX), a Bruker ER 4122 SHQE cavity and an Oxford Instruments Helium-gas continuous flow cryostat (ESR900).

A conventional field-modulation technique combined with lock-in detection has been used for measurements in the dark and under continuous illumination, which resulted in the first derivative of the EPR absorption spectra. For the experiment conducted under synchronously modulated illumination the magnetic field modulation has been substituted by modulation of light, once again combined with lock-in detection. The latter scheme yielded directly the EPR absorption signal instead of its first derivative as for conventional measurements performed either in the dark or under continuous illumination. Such an approach, while taking advantage of the lock-in detection technique, has been chosen to highlight the light-induced changes. The working principles of the two methods are shown in more detail in figure S6.

2.7. Light sources for illumination of the nanohybrid samples

Illumination for field-modulated EPR measurements (i.e. for light-on spectra) was provided by different light sources: (i) a green, $\lambda = 532$ nm laser at an illumination power of 20 mW (Laser Quantum Ltd.) (ii) by a red, $\lambda = 660$ nm, 50 mW AlGaInP laser diode (ADL-66505TL); (iii) by a halogen lamp; or by (iv) an ultraviolet lamp with an illumination intensity of 20 or 40 mW.

The illumination for light-modulated EPR measurements was provided by a red, $\lambda = 660$ nm, 50 mW AlGaInP laser diode (ADL-66505TL). The light modulation was performed using an Agilent 33250A 80 MHz Function/Arbitrary Waveform Generator.

Calibration of the light intensity was performed by connecting a calibrated photodiode to a Stanford Research Systems model SR830 DSP lock-in.

3. Results and discussion

3.1. MAPbI$_3$/blue-TiO$_2$NWs-based visible light photodetector

To prove the concept of enhanced light-induced charge transfer at the MAPbI$_3$/blue-TiO$_2$NWs interface, we designed a visible light photodetector. To this end, a single crystal of MAPbI$_3$ was brought into electrical contact by dry-pressing (described in detail in [43]) with a pellet made of either blue-TiO$_2$NWs or white-TiO$_2$NWs.

The photographic images of the starting material for preparation of TiO$_2$NWs pellets, i.e. protonated layered titanate H$_2$Ti$_3$O$_7$ nanowires (TiO$_2$NWs), as well as thermally-reduced (blue-TiO$_2$NWs) and thermally re-oxidized TiO$_2$NWs (white-TiO$_2$NWs), are shown in figure 1(a). As can be seen, thermal reduction in hydrogen atmosphere at 600 °C transforms the original white-coloured powder of TiO$_2$NWs into a blue-coloured powder (blue-TiO$_2$NWs). The subsequent calcination in air at either 450 °C or 550 °C converts blue-TiO$_2$NWs back to the white-coloured material (white-TiO$_2$NWs). Hereinafter, the two versions of the latter re-oxidized material are referred to as white-TiO$_2$NWs(450 °C) and white-TiO$_2$NWs(550 °C), respectively.

We have shown previously that blue-TiO$_2$NWs and both white-TiO$_2$NWs(450 °C) and white-TiO$_2$NWs(550 °C) reveal the same anatase-like crystal structure [37]. The major difference between the reduced (blue-TiO$_2$NWs) and re-oxidized (white-TiO$_2$NWs) versions of this material is in their content of paramagnetic Ti^{3+} surface states, which is at least three orders of magnitude higher for blue-TiO$_2$NWs, thus reaching ~1% of the total concentration of the surface titanium ions [37].

The schematic band structure diagram at the MAPbI$_3$/blue-TiO$_2$NWs interface is shown in figure 1(c). As indicated, the population of Ti^{3+} surface states provides shallow donor levels located from 0.3 to 0.7 eV below the conduction band (CB) minimum of TiO$_2$ [44, 45]. It has been generally accepted that these Ti^{3+} species are occupied states and usually act as donors, thus largely contributing to the improved electrical conductivity of blue-TiO$_2$NWs. The electrons in these sites can be excited into the CB either by a thermal or photoexcitation process to form the unoccupied states [46, 47]. Correspondingly, the herein observed marked colour change can also be ascribed to enhanced absorption of the visible and near-infrared light by Ti^{3+} surface states in blue-TiO$_2$NWs [48].

The I–V characteristics acquired under visible light illumination for the described simple photodetector are shown in figure 1(b). The scheme of the MAPbI$_3$/TiO$_2$ photo-junction is shown in the inset to figure 1(b). All the I–V characteristics exhibited a diode-like behaviour for three different materials used to form the TiO$_2$NWs pellets, i.e. blue-TiO$_2$NWs, white-TiO$_2$NWs(450 °C) and white-TiO$_2$NWs(550 °C). However, both the forward

Figure 1. (a) Photographic images of TiO$_2$NWs powders at different stages of thermal treatment: the starting material, TiO$_2$NWs, i.e. protonated layered titanate H$_2$Ti$_3$O$_7$ nanowires (left), thermally-reduced blue-TiO$_2$NWs (middle) and re-oxidized by calcination in air white-TiO$_2$NWs (right). (b) Comparison of the *I–V* characteristics collected under the visible light illumination for three variants of the MAPbI$_3$/TiO$_2$ junctions: MAPbI$_3$/blue-TiO$_2$NWs (blue squares), MAPbI$_3$/white-TiO$_2$NWs(450 °C) (red squares) and MAPbI$_3$/white-TiO$_2$NWs(550 °C) (green squares). Inset: simplified drawing showing the experimental setup for acquiring the *I–V* curves consisting of a MAPbI$_3$ single crystal brought into contact with a TiO$_2$NWs pellet and of two tungsten needles providing the electrical contacts. (c) Schematic representation of the energy band alignment diagram at the MAPbI$_3$/blue-TiO$_2$NWs interface. (d) Comparison of the *light on—light off* photo-current transient trains for three variants of the MAPbI$_3$/TiO$_2$ junctions: MAPbI$_3$/blue-TiO$_2$NWs (blue trace), MAPbI$_3$/white-TiO$_2$NWs(450 °C) (red trace) and MAPbI$_3$/white-TiO$_2$NWs(550 °C) (green trace).
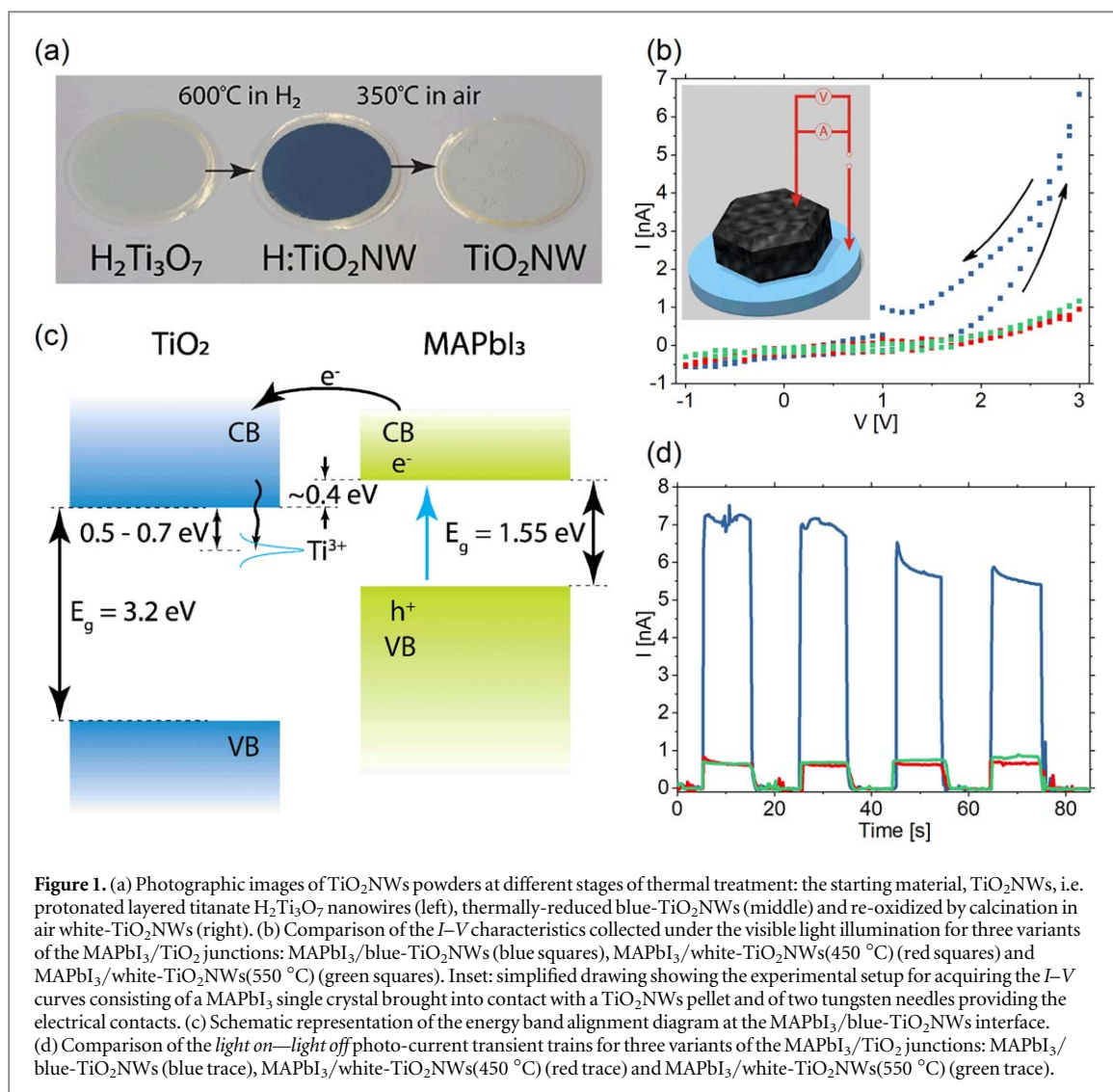
photo-current and the rectification ratio were markedly superior for the device consisting of a single MAPbI$_3$ crystal brought into electrical contact with the pellet made of blue-TiO$_2$NWs. The *I–V* characteristics collected for the devices employing the pellets made of either white-TiO$_2$NWs(450 °C) or white-TiO$_2$NWs(550 °C), were practically identical. This observation suggests that the charge transport properties of white-TiO$_2$NWs do not differ significantly for the material calcinated at either 450 °C or 550 °C. The hysteretic character of the recorded *I–V* curves can be ascribed to the presence of mobile ions and their slow migration through the perovskite material, as reported earlier [49, 50].

In figure 1(d), we show the corresponding photo-current transients, whereby illumination with the visible light was consecutively turned *on* and *off*. The strongest responses to the dark-light illumination conditions were observed for the photo-junction consisting of a single MAPbI$_3$ crystal and the pellet made of blue-TiO$_2$NWs. Notwithstanding, the rise times are similar for all the photo-junctions, being of ∼0.1 s. In contrast, the fall times are different, being of ∼1.0 s and ∼1.8 s, for photo-junctions employing blue-TiO$_2$NWs and white-TiO$_2$NWs, respectively. Shorter fall times observed for the photo-junction employing blue-TiO$_2$NWs can be explained by a larger concentration of shallow donor traps in the thermally-reduced TiO$_2$NWs, which leads to faster recombination of the injected charges.

3.2. Quantification of the charge transfer at the MAPbI$_3$/blue-TiO$_2$NWs interface: a photo-EPR study

To quantify the effect of the charge transfer at the interface between MAPbI$_3$ and TiO$_2$ and to gain insight into the underlying mechanisms, we performed low-temperature Photo-EPR measurements on a model nanohybrid system consisting of blue-TiO$_2$NWs dispersed in a polycrystalline MAPbI$_3$ matrix. In this approach, thermally-reduced TiO$_2$NWs (blue-TiO$_2$NWs), containing a large concentration of paramagnetic species of trivalent titanium (Ti^{3+}, $S = 1/2$), was used as a model for the ETL. Moreover, the dispersion of blue-TiO$_2$NWs in polycrystalline MAPbI$_3$ ensured a large distributed surface of the MAPbI$_3$/blue-TiO$_2$NWs interface.
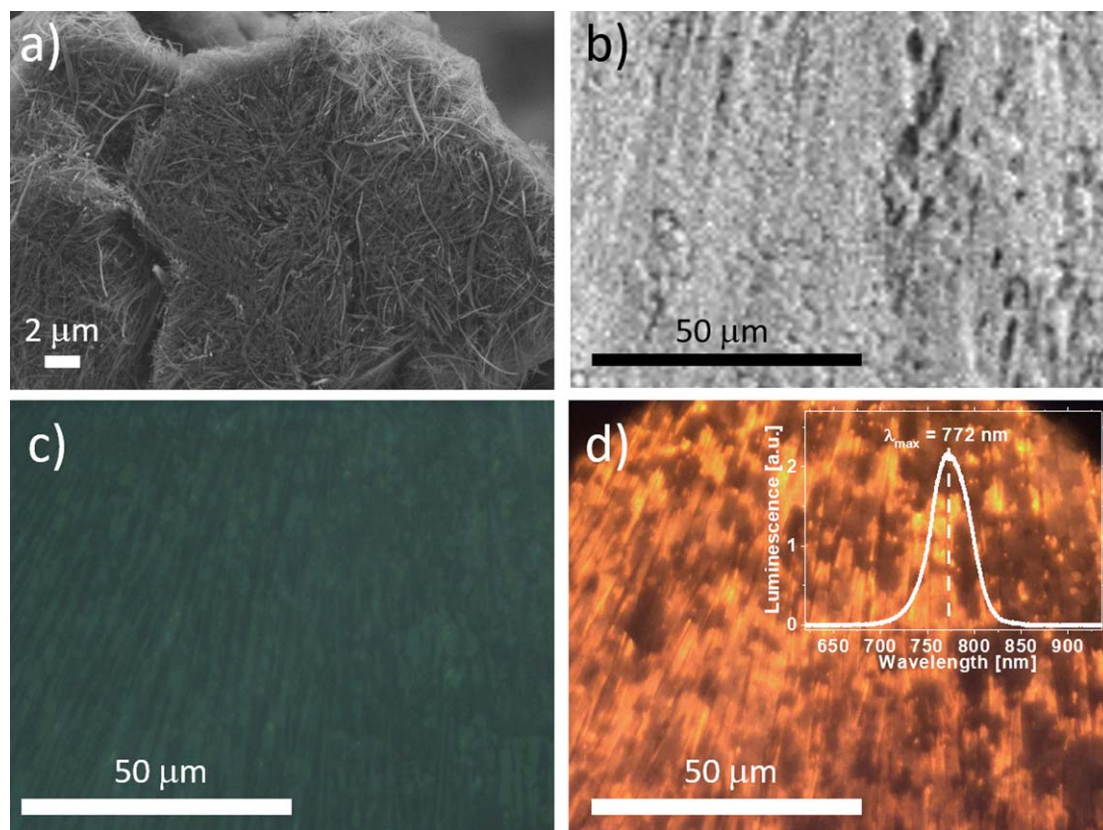
Figure 2. Morphological characterization of the MAPbI$_3$/blue-TiO$_2$NWs nanohybrid. (a) SEM image of the blue-TiO$_2$NWs deposit. (b) SEM, (c) optical and (d) fluorescence (under λ_{exc} = 546 nm excitation) images of the MAPbI$_3$/blue-TiO$_2$NWs nanohybrid showing the MAPbI$_3$ wire-like morphology and inclusions of blue-TiO$_2$NWs. Inset: photoluminescence spectrum acquired for the MAPbI$_3$/blue-TiO$_2$NWs nanohybrid material.

The morphological characterization of blue-TiO$_2$NWs and the MAPbI$_3$/blue-TiO$_2$NWs nanohybrid material is presented in figure 2. Specifically, figure 2(a) shows the SEM image of the thin deposit consisting solely of blue-TiO$_2$NWs. Blue-TiO$_2$NWs form a highly interlaced pattern in a thin-film deposit, while an individual blue-TiO$_2$NW, has a large length-to-width aspect ratio, with ∼5–10 μm in length and ∼10 nm in width.

Subsequently, the morphological features of the MAPbI$_3$/blue-TiO$_2$NWs nanohybrid material are shown in figures 2(b)–(d). In particular, the presence of blue-TiO$_2$NWs can be concluded from the SEM image of the nanohybrid material (figure 2(b)). Although, due to a big difference in sizes, this SEM image is dominated by markedly bigger MAPbI$_3$ microwires, numerous agglomerates of blue-TiO$_2$NWs can also be seen. They form randomly distributed protuberances on the relatively regular pattern of MAPbI$_3$ microwires.

At the same time SEM element analysis, seen in figure S1 was performed for three elements seen as an overlap over an SEM image in figure S1(a) and found as an element distribution histogram in figure S1(b). Separate element distribution maps are also presented for iodine (figure S1(c)), lead (figure S1(d)) and titanium (figure S1(e)), the first two corresponding to the distributions of MAPbI$_3$ and the latter to the distribution of blue-TiO$_2$NWs in a MAPbI$_3$/blue-TiO$_2$NWs nanohybrid deposit. These element maps clearly show a homogeneous distribution of the three above-mentioned elements providing further evidence of homogeneous spread of blue-TiO$_2$NWs on MAPbI$_3$ microwires.

The inclusions of blue-TiO$_2$NWs are also visible in the optical microscopy and fluorescence images (figures 2(c) and (d)). In particular, in the fluorescence image acquired under λ_{exc} = 546 nm excitation, agglomerates of blue-TiO$_2$NWs can be seen as darker spots that partially overlap the luminescent microwires of MAPbI$_3$ (figure 2(d)). The corresponding relatively narrow luminescence spectrum, peaking at 772 nm (FWHM = 48 nm), is typical for thin deposits of polycrystalline MAPbI$_3$.

It is noteworthy to mention that thin-film deposits of MAPbI$_3$ coated by single-step solution casting from neat DMF solutions very often appear to show microwire- or fibre-like surface morphology [51]. We also have previously reported similar microwire-like morphology and practically identical luminescence characteristics for single-step solution cast deposits of MAPbI$_3$ on various types of both curved and flat substrates (microwires with sizes of ∼8 μm in diameter and up to ∼150 μm in length were observed for small substrates' curvatures or
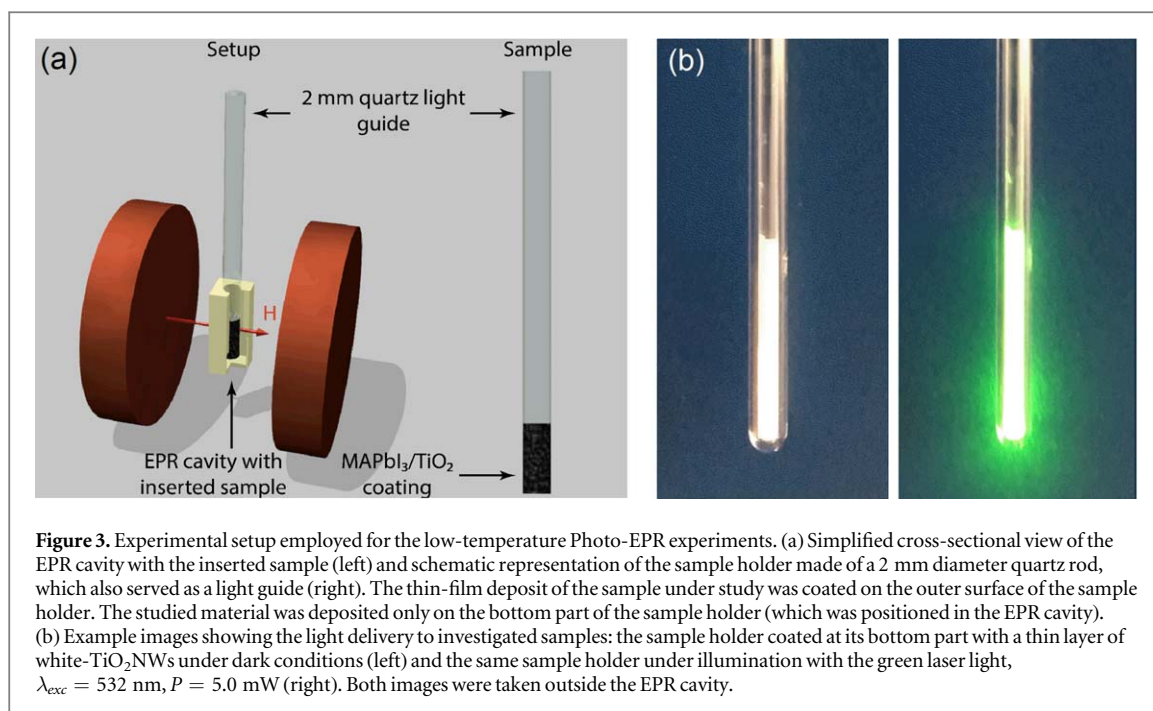
Figure 3. Experimental setup employed for the low-temperature Photo-EPR experiments. (a) Simplified cross-sectional view of the EPR cavity with the inserted sample (left) and schematic representation of the sample holder made of a 2 mm diameter quartz rod, which also served as a light guide (right). The thin-film deposit of the sample under study was coated on the outer surface of the sample holder. The studied material was deposited only on the bottom part of the sample holder (which was positioned in the EPR cavity). (b) Example images showing the light delivery to investigated samples: the sample holder coated at its bottom part with a thin layer of white-TiO_2NWs under dark conditions (left) and the same sample holder under illumination with the green laser light, $\lambda_{exc} = 532$ nm, $P = 5.0$ mW (right). Both images were taken outside the EPR cavity.

flat surfaces) [52]. Therefore, one can conclude that the presence of blue-TiO_2NWs does not significantly modify nucleation and crystal growth of $MAPbI_3$ microwires during deposition of the $MAPbI_3$/blue-TiO_2NWs nanohybrid from stoichiometric solutions of $MAPbI_3$ in DMF (for more details see section 2 and supplementary material, available online at stacks.iop.org/JPPHOTON/2/014007/mmedia).

The experimental setup used for low-temperature Photo-EPR measurements oriented towards the detection and quantization of photo-generated charges at the $MAPbI_3$/blue-TiO_2NWs interface is depicted in figure 3. As schematically shown, a 2 mm diameter rod made of clear fused quartz was implemented to position the sample and deliver light into the EPR cylindrical cavity (TE_{011}) resonator (figure 3(a)). The deposits of all the studied materials, including the $MAPbI_3$/blue-TiO_2NWs nanohybrid, were directly coated on the outer surface of the quartz rod by dip-coating. Only the bottom part of the quartz rod, which protruded into the EPR resonator, was coated. Thin-film deposits of the commercially available anatase (AMT600, Tayca Corp.), as well as of white-TiO_2NWs and blue-TiO_2NWs, suspensions in ethanol incorporating also small amounts of polyethylene oxide (PEO) and water (10%), while, as discussed above, the $MAPbI_3$/blue-TiO_2NWs nanohybrid was coated from the stoichiometric solution of $MAPbI_3$ in DMF, which contained suspended blue-TiO_2NWs (for more details see section 2 and supplementary material).

Due to a substantial difference in refractive indices between $MAPbI_3$ ($n \approx 2.8$) [39], TiO_2 ($n \approx 2.6$) [40] and quartz ($n \approx 1.46$) [41] our approach made it possible to efficiently extract light from the quartz light guide to the whole surface of the deposited material. Figure 3(b) provides exemplary proof of very efficient extraction of the green laser light ($\lambda_{exc} = 532$ nm) from the quartz-made sample holder to a thin deposit of white-TiO_2NWs.

The most important findings of this work stemming from the low-temperature Photo-EPR study of photo-generated charges at the model MHP/ETL interface are summarized in figure 4.

The comparative EPR evaluation of three TiO_2-based materials having the potential for applications in a model $MAPbI_3$/TiO_2 system is shown in figure 4(a). Specifically, the stacked plot in this figure compiles normalized EPR spectra acquired at 20 K for the commercially available anatase (black trace), white-TiO_2NWs (red trace) and blue-TiO_2NWs (blue trace).

Although all three spectra reveal the presence of paramagnetic species, it can be concluded that blue-TiO_2NWs provide the strongest EPR-detectable feature (blue trace). In particular, as discussed in details in [53], the strong EPR signal observed for blue-TiO_2NWs corresponds to a powder EPR spectrum of the surface-located Ti^{3+} paramagnetic centers. We demonstrate our general approach to study the interface using the blue-TiO_2NWs due to the large Ti^{3+} surface defect concentration and the corresponding large EPR signal intensity. For distorted (tetragonally-elongated) octahedral sites this signal can be fitted with a uniaxial powder distribution having two *g*-factor components: parallel ($g_{\parallel} = 1.94$) and perpendicular ($g_{\perp} = 1.97$) ([53] and references therein). The temperature dependence of the EPR signal intensity confirmed the Curie-type behaviour for these Ti^{3+}-related paramagnetic centers in blue-TiO_2NWs (see supplementary material, figure S4.). The overall concentration of paramagnetic Ti^{3+} centers in blue-TiO_2NWs, estimated in our previous publication, was found to be of ~0.4% of all the surface Ti cations [37].
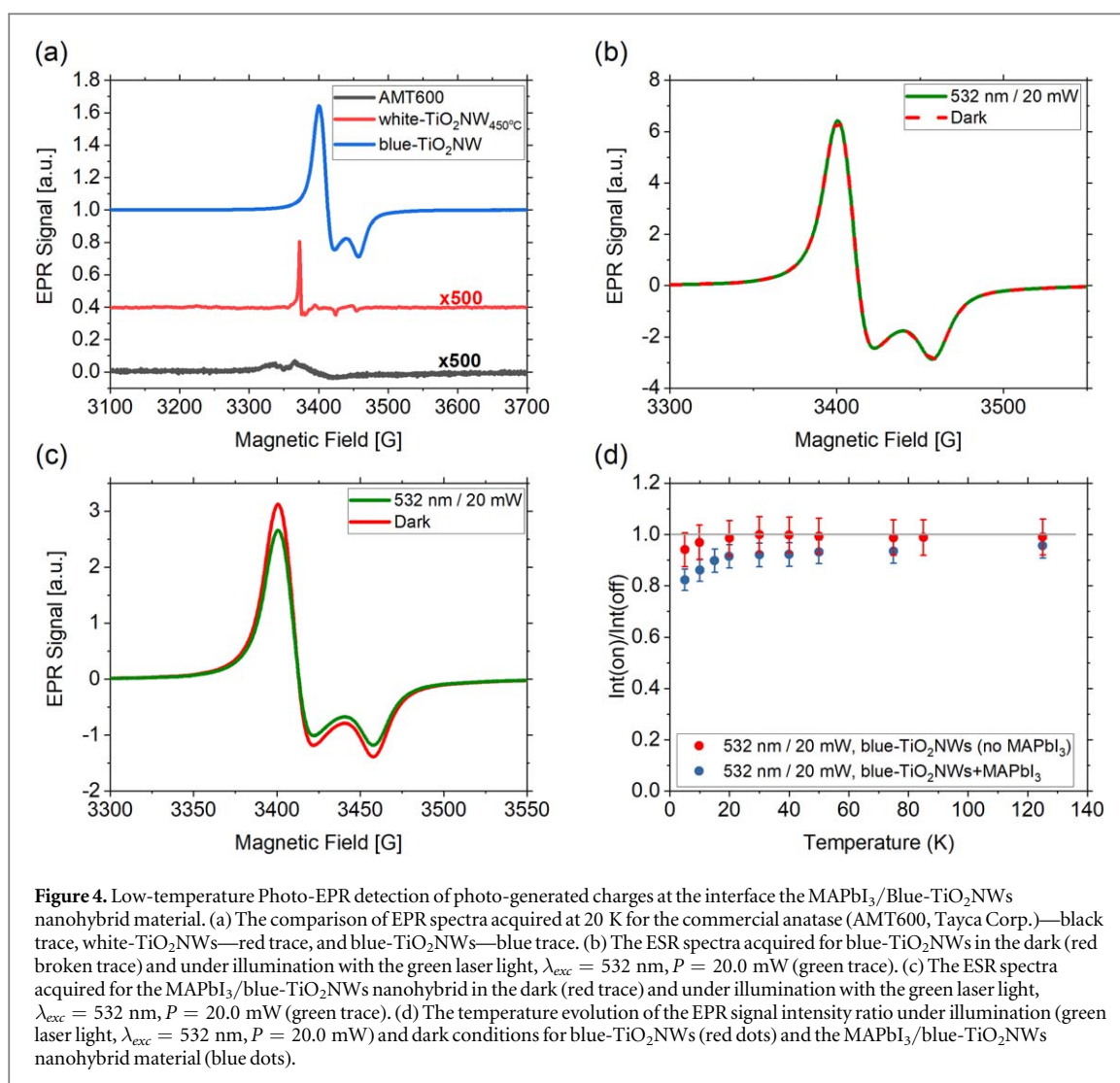
Figure 4. Low-temperature Photo-EPR detection of photo-generated charges at the interface the MAPbI$_3$/Blue-TiO$_2$NWs nanohybrid material. (a) The comparison of EPR spectra acquired at 20 K for the commercial anatase (AMT600, Tayca Corp.)—black trace, white-TiO$_2$NWs—red trace, and blue-TiO$_2$NWs—blue trace. (b) The ESR spectra acquired for blue-TiO$_2$NWs in the dark (red broken trace) and under illumination with the green laser light, $\lambda_{exc} = 532$ nm, $P = 20.0$ mW (green trace). (c) The ESR spectra acquired for the MAPbI$_3$/blue-TiO$_2$NWs nanohybrid in the dark (red trace) and under illumination with the green laser light, $\lambda_{exc} = 532$ nm, $P = 20.0$ mW (green trace). (d) The temperature evolution of the EPR signal intensity ratio under illumination (green laser light, $\lambda_{exc} = 532$ nm, $P = 20.0$ mW) and dark conditions for blue-TiO$_2$NWs (red dots) and the MAPbI$_3$/blue-TiO$_2$NWs nanohybrid material (blue dots).

The much weaker EPR spectrum recorded for white-TiO$_2$NWs (red trace) can be interpreted as originating mostly from paramagnetic oxygen vacancies, V_O^- (the narrow peak at $g \approx 2.003$) [54], and a low concentration of bulk-located Ti^{3+} centers (at g-factor values of ≈ 1.99 and ≈ 1.96).

Interestingly, the traces of Ti^{3+} paramagnetic centers can also be observed for the untreated commercial anatase (weak signals at g-factor values of ≈ 1.97 and ≈ 1.94). However, the overall EPR spectrum of this material (black trace) is clearly dominated by a broadened signal with g-factor values of ≈ 2.029, ≈ 2.011 and ≈ 2.003, which can be ascribed to the adsorbed reduced oxygen molecules and structural oxygen species, i.e. superoxide and oxygen ($O_2^-/O^{\cdot-}$) radicals [55, 56].

Figure 4(b) reports the EPR spectra acquired for the deposit of blue-TiO$_2$NWs under illumination with the green laser light ($\lambda_{exc} = 532$ nm, $P = 20.0$ mW) and dark conditions. In the present study, this sample, consisting solely of the thermally-reduced TiO$_2$NWs, served as a reference for the MAPbI$_3$/blue-TiO$_2$NWs nanohybrid material. It can be seen that the EPR spectra recorded for blue-TiO$_2$NWs in the dark and under illumination perfectly overlap each other. As discussed before, both ESR spectra correspond to Ti^{3+} paramagnetic centers with their characteristic powder distribution with g-factor values of $g_\parallel = 1.94$ and $g_\perp = 1.97$.

In contrast, as shown in figure 4(c), the EPR signal of Ti^{3+} centers in the thin-film deposit of the MAPbI$_3$/blue-TiO$_2$NWs nanohybrid material markedly diminishes under identical illumination conditions. Thus, the observed reduction of the EPR signal upon illumination can be associated with the transfer of photo-excited electrons from MAPbI$_3$ to blue-TiO$_2$NWs. In particular, the light-excited non-equilibrium electrons in MAPbI$_3$ cross the interface at grain boundaries between MAPbI$_3$ polycrystals and dispersed blue-TiO$_2$NWs, thus leading to conversion of Ti^{3+} EPR-active centers (d^1, $S = 1/2$) to EPR-silent Ti^{2+} states (d^2, $S = 0$). The light-induced drop in the EPR signal intensity for the herein studied MAPbI$_3$/blue-TiO$_2$NWs nanohybrid material was $\sim 20\%$ at 20 K.

Temperature evolutions of the EPR-detected charge transfer for the deposit of MAPbI$_3$/blue-TiO$_2$NWs nanohybrid material and the reference sample, i.e. the deposit consisting solely of blue-TiO$_2$NWs, are shown in figure 4(d). It can be seen that the ratio of the EPR signal intensities acquired for the deposit of MAPbI$_3$/blue-TiO$_2$NWs nanohybrid material under illumination and dark conditions is markedly lower than unity, adapting values from ∼0.8 to ∼0.9 in the temperature range of 5–80 K (blue dots). In contrast, the corresponding EPR signal intensity ratio for the reference sample remains close to unity and is practically independent of temperature (red dots). It is worth mentioning that with increasing temperatures the line-width of the Ti^{3+}-related EPR signal rapidly broadens up, thus rendering difficult the EPR measurements at temperatures higher than 100 K (for details see supplementary material, figure S4).

The observed light-induced changes were fully reversible and the EPR signal recovered its initial amplitude under dark conditions. This phenomenon was observed for the MAPbI$_3$/blue-TiO$_2$NWs nanohybrid deposit under illumination at different wavelengths. However, the most prominent effect, corresponding to ca. 20% drop of the ESR signal intensity, occurred under illumination with the green laser light (λ_{exc} = 532 nm).

As can be deduced from the band structure diagram of the MAPbI$_3$/blue-TiO$_2$NWs interface (figure 1(c)), the photon energy at this wavelength (2.33 eV) is lower than the energy of intraband Ti^{3+} states, which are located ca. 0.5–0.7 eV below the edge of the CB of TiO$_2$. Therefore, the light-induced excitation under illumination at 532 nm wavelength takes place within the narrow-band semiconductor, MAPbI$_3$, whereas blue-TiO$_2$NWs serve as a unidirectional electron sink with an enhanced electron trapping efficiency due to the presence of Ti^{3+} species.

Since our experimental setup was not optimized for performing time-resolved Photo-EPR experiments, we also performed an additional experiment in which the standard modulation of the magnetic field was replaced by modulation of the light source. This approach made it possible to excite the investigated sample with intensity-modulated light using modulation frequencies in the range 1–50 kHz (for details see supplementary material). Based on this procedure, we found that both the light-induced ESR signal decay and its recovery in the dark were faster than the experimental frequency limit of the light modulation (∼50 kHz), thus shorter than 20 µs.

3.3. Conclusions

Taken together, we report a contactless method to directly track photo-carriers at the ETL/MHP interface in a model system consisting of TiO$_2$-based nanowires (TiO$_2$NWs) dispersed in the polycrystalline MAPbI$_3$ matrix. Specifically, thermally-reduced TiO$_2$NWs (blue-TiO$_2$NWs), containing a large concentration of Ti^{3+} paramagnetic centers, were used as the representative material for the ETL. The dispersion of blue-TiO$_2$NWs in polycrystalline MAPbI$_3$ ensured a large distributed surface of the MAPbI$_3$/blue-TiO$_2$NWs interface.

The technique of low-temperature EPR in combination with *in situ* illuminations (Photo-EPR) was implemented to monitor the light-induced changes in concentration of Ti^{3+} paramagnetic centers in blue-TiO$_2$NWs. In particular, we find that under illumination with the green laser light (λ_{exc} = 532 nm) the concentration of Ti^{3+} species in blue-TiO$_2$NWs drops by ca. 20%. This process can be understood in terms of the transfer of light-excited non-equilibrium electrons from MAPbI$_3$ to blue-TiO$_2$NWs, which in turn leads to conversion of EPR-active Ti^{3+} centers (d^1, S = 1/2) to EPR-silent Ti^{2+} states (d^2, S = 0).

It is also worth noting that the above-mentioned results, stemming from low-temperature Photo-EPR measurements, corroborate the findings for a model ETL/MHP junction, which was formed by bringing into contact the compacted powder of TiO$_2$NWs with a single crystal of MAPbI$_3$. In particular, based on the *I–V* characteristics of such a simple light detector, we show that both the forward photo-current and the rectification ratio were markedly improved when the compacted powder of blue-TiO$_2$NWs (reduced, containing Ti^{3+} species) was used as the model ETL as compared to the compacted white-TiO$_2$NWs (thermally re-oxidized).

Thus, for the herein studied model ETL/MHP interface, both the low-temperature Photo-EPR measurements and the results obtained for a simple light detector confirm that blue-TiO$_2$NWs serve as a unidirectional electron sink with an enhanced electron trapping efficiency due to the presence of Ti^{3+} species.

Overall, we also infer that the technique of low-temperature Photo-EPR is an effective strategy to study the transfer mechanisms of photogenerated carriers at the ETL/MHP interface in MAPbI$_3$-based photovoltaic and photoelectronic systems.

Acknowledgments

ORCID iDs

Konstantins Mantulnikovs ● https://orcid.org/0000-0002-3053-7605
Péter Szirmai ● https://orcid.org/0000-0002-2841-5692
Márton Kollár ● https://orcid.org/0000-0001-9335-2715
Andrzej Sienkiewicz ● https://orcid.org/0000-0003-3527-7379

References

[1] Yusoff A R B M and Nazeeruddin M K 2016 *J. Phys. Chem. Lett.* **7** 851–66
[2] Ghosh J, Ghosh R and Giri P K 2018 *ACS Appl. Nano Mater.* **1** 1551–62
[3] Ghosh J, Ghosh R and Giri P K 2019 *ACS Appl. Mater. Interfaces* **11** 14917–31
[4] Fan J, Jia B and Gu M 2014 *Photonics Res.* **2** 111–20
[5] Veldhuis S A, Boix P P, Yantara N, Li M, Sum T C, Mathews N and Mhaisalkar S G 2016 *Adv. Mater.* **28** 6804–34
[6] Cho H *et al* 2015 *Science* **350** 1222–5
[7] Kojima A, Teshima K, Shirai Y and Miyasaka T 2009 *J. Am. Chem. Soc.* **131** 6050–1
[8] Kim H S *et al* 2012 *Sci. Rep.* **2** 591
[9] 2019 2018 Nrel efficiency chart Online (accessed 28 Dec 2019) (https://nrel.gov/pv/assets/pdfs/best-research-cell-efficiencies. 20191106.pdf)
[10] Náfrádi B, Náfrádi G, Forró L and Horváth E 2015 *J. Phys. Chem.* C **119** 25204–8
[11] Andričević P, Kollár M, Mettan X, Náfrádi B, Sienkiewicz A, Fejes D, Hernádi K, Forró L and Horváth E 2017 *J. Phys. Chem.* C **121** 13549–56
[12] Spina M, Lehmann M, Náfrádi B, Bernard L, Bonvin E, Gaál R, Magrez A, Forró L and Horváth E 2015 *Small* **11** 4824–8
[13] Zhang M, Zhang F, Wang Y, Zhu L, Hu Y, Lou Z, Hou Y and Teng F 2018 *Sci. Rep.* **8** 11157
[14] Saraf R, Pu L and Maheshwari V 2018 *Adv. Mater.* **30** 1705778
[15] Bao C, Yang J, Zhu W, Zhou X, Gao H, Li F, Fu G, Yu T and Zou Z 2015 *Chem. Commun.* **51** 15426–9
[16] Yakunin S, Dirin D N, Shynkarenko Y, Morad V, Cherniukh I, Nazarenko O, Kreil D, Nauser T and Kovalenko M V 2016 *Nat. Photonics* **10** 585–9
[17] Habisreutinger S N, Leijtens T, Eperon G E, Stranks S D, Nicholas R J and Snaith H J 2014 *Nano Lett.* **14** 5561–8
[18] Spina M, Nafradi B, Tohati H M, Kamaras K, Bonvin E, Gaal R, Forro L and Horvath E 2016 *Nanoscale* **8** 4888–93
[19] Tohati H M, Pekker A, Andricevic P, Forro L, Nafradi B, Kollar M, Horvath E and Kamaras K 2017 *Nanoscale* **9** 17781–7
[20] Andričević P, Mettan X, Kollár M, Náfrádi B, Sienkiewicz A, Garma T, Rossi L, Forró L and Horváth E 2019 *ACS Photonics* **6** 967–75
[21] Ghosh J, Natu G and Giri P 2019 *Org. Electron.* **71** 175–84
[22] Ranjan R, Prakash A, Singh A, Singh A, Garg A and Gupta R K 2018 *J. Mater. Chem.* A **6** 1037–47
[23] Umebayashi T, Yamaki T, Itoh H and Asai K 2002 *J. Phys. Chem. Solids* **63** 1909–20
[24] Teruhisa O, Takahiro M and Michio M 2003 *Chem. Lett.* **32** 364–5
[25] Murphy A 2008 *Sol. Energy Mater. Sol. Cells* **92** 363–7
[26] Paramasivam I, Macak J and Schmuki P 2008 *Electrochem. Commun.* **10** 71–5
[27] Ghafoor S, Ata S, Mahmood N and Arshad S N 2017 *Sci. Rep.* **7** 255
[28] Xue J, Shen Q, Liang W, Liu X and Yang F 2013 *Electrochim. Acta* **97** 10–6
[29] Pérez-del Rey D, Boix P P, Sessolo M, Hadipour A and Bolink H J 2018 *J. Phys. Chem. Lett.* **9** 1041–6
[30] Momblona C, Gil-Escrig L, Bandiello E, Hutter E M, Sessolo M, Lederer K, Blochwitz-Nimoth J and Bolink H J 2016 *Energy Environ. Sci.* **9** 3456–63
[31] Dunlap-Shohl W A, Li T and Mitzi D B 2019 *Appl. Energy Mater.* **2** 5083–93
[32] Hutter E M, Hofman J J, Petrus M L, Moes M, Abellón R D, Docampo P and Savenije T J 2017 *Adv. Energy Mater.* **7** 1602349
[33] Ishida N, Wakamiya A and Saeki A 2016 *ACS Photonics* **3** 1678–88
[34] Ponseca C S, Hutter E M, Piatkowski P, Cohen B, Pascher T, Douhal A, Yartsev A, Sundström V and Savenije T J 2015 *J. Am. Chem. Soc.* **137** 16043–8
[35] Peng J, Chen Y, Zheng K, Pullerits T and Liang Z 2017 *Chem. Soc. Rev.* **46** 5714–29
[36] Tétreault N *et al* 2010 *ACS Nano* **4** 7644–50
[37] Szirmai P *et al* 2017 *Catal. Today* **284** 52–8
[38] Berger H, Tang H and Lévy F 1993 *J. Cryst. Growth* **130** 108–12
[39] Löper P, Stuckelberger M, Niesen B, Werner J, Filipič M, Moon S J, Yum J H, Topič M, De Wolf S and Ballif C 2015 *J. Phys. Chem. Lett.* **6** 66–71
[40] DeVore J R 1951 *J. Opt. Soc. Am.* **41** 416–9
[41] Ghosh G 1999 *Opt. Commun.* **163** 95–102
[42] Náfrádi B, Szirmai P, Spina M, Lee H, Yazyev O V, Arakcheeva A, Chernyshov D, Gibert M, Forró L and Horváth E 2016 *Nat. Commun.* **7** 13406
[43] Vujančević J *et al* 2019 *Ceram. Int.* **45** 10013–20
[44] Amano F, Nakata M, Yamamoto A and Tanaka T 2016 *J. Phys. Chem.* C **120** 6467–74
[45] Liu W, Butté R, Dussaigne A, Grandjean N, Deveaud B and Jacopin G 2016 *Phys. Rev.* B **94** 195411
[46] Lisachenko A A, Mikhailov R V, Basov L L, Shelimov B N and Che M 2007 *J. Phys. Chem.* C **111** 14440–7
[47] Panayotov D A and Yates J T 2007 *Chem. Phys. Lett.* **436** 204–8
[48] Ou G *et al* 2018 *Nat. Commun.* **9** 1302
[49] Yi H T, Wu X, Zhu X and Podzorov V 2016 *Adv. Mater.* **28** 6509–14
[50] Unger E L, Hoke E T, Bailie C D, Nguyen W H, Bowring A R, Heumüller T, Christoforo M G and McGehee M D 2014 *Energy Environ. Sci.* **7** 3690–8
[51] Jung M, Ji S G, Kim G and Seok S I 2019 *Chem. Soc. Rev.* **48** 2011–38
[52] Mantulnikovs K, Glushkova A, Matus P, Ćirić, L, Kollár M, Forró L, Horváth E and Sienkiewicz A 2018 *ACS Photonics* **5** 1476–85
[53] Szirmai P, Fábián G, Dóra B, Koltai J, Zólyomi V, Kürti J, Nemes N M, Forró L and Simon F 2011 *Phys. Status Solidi* b **248** 2688–91
[54] Nakamura I, Negishi N, Kutsuna S, Ihara T, Sugihara S and Takeuchi K 2000 *J. Mol. Catal.* A **161** 205–12
[55] Carter E, Carley A F and Murphy D M 2007 *J. Phys. Chem.* C **111** 10630–8
[56] Pan X and Xu Y J 2013 *J. Phys. Chem.* C **117** 17996–8005